# Characteristics of a plasma sheath in a magnetic dipole field: Implications to the solar wind interaction with the lunar magnetic anomalies

X. Wang,[1,2] M. Horányi,[1,2,3] and S. Robertson[2,3]

Received 18 February 2012; revised 8 May 2012; accepted 16 May 2012; published 27 June 2012.

[1] The solar wind interaction with the lunar surface, especially in regions of crustal magnetic anomalies, remains of great interest for in situ plasma measurements. Small- scale laboratory experiments cannot reproduce the conditions near the lunar surface, but provide a unique opportunity to identify and examine several of the physical processes. We study plasma interaction with a magnetic dipole field at an insulating surface in order to understand the effect of crustal magnetic anomalies on the solar wind–lunar surface interaction. In our experiments, electrons are magnetized with gyroradii $r$ smaller than distances from the surface $d$ ($r < d$) but ions remain unmagnetized with $r > d$. The measured potential distribution shows a non-monotonic sheath above the surface and variations on the surface along the axis of the dipole field. The surface near the center of the dipole is charged more positively by ions as the electrons are magnetically shielded away. A potential minimum is found in the shielding region between the surface and the bulk plasma due to collisional and magnetic mirror trapping effects. Potential variations on the surface are the result of the inhomogeneity of the dipolar field, showing an enhancement of the electric field at the cusps. Enhanced electric fields in the regions of magnetic anomalies on the lunar surface may enhance the transport of small-sized charged dust particles, possibly explaining the formation of the lunar swirls.

**Citation:** Wang, X., M. Horányi, and S. Robertson (2012), Characteristics of a plasma sheath in a magnetic dipole field: Implications to the solar wind interaction with the lunar magnetic anomalies, *J. Geophys. Res.*, *117*, A06226, doi:10.1029/2012JA017635.

## 1. Introduction

[2] The Moon has a thin atmosphere/exosphere and no global magnetic field. Earlier measurements back to Apollo era have inferred the absence of a global or significant large-scale magnetic field at the Moon by the absence of a standing shock wave in the solar wind upstream from the Moon as well as at the limb of the Moon [*Colburn et al.*, 1967, 1971; *Lyon et al.*, 1967; *Ness et al.*, 1967, 1968; *Taylor et al.*, 1968]. Rather, limits on the scale sizes of the lunar fields were indicated from both the Apollo surface measurements [*Dyal et al.*, 1971] and orbiter observations [*Barnes et al.*, 1971]. These small-scale magnetic fields, called magnetic anomalies, are regions of crustal magnetization distributed over the lunar surface. Recent in situ measurements show that these local magnetic fields can be as high as 30 nT at 20–30 km altitude and as high as several hundred nT at the surface, and range in size from less than a km to hundreds of km [*Halekas et al.*, 2001; *Hood et al.*, 2001; *Mitchell et al.*, 2008]. Studies have shown that the lunar magnetic anomalies may have strong influence on the solar wind flow. Magnetic enhancements detected at lunar limbs were explained by a shock-like interaction of the solar wind with strong crustal magnetic fields [*Russell and Lichtenstein*, 1975; *Lin et al.*, 1998; *Halekas et al.*, 2006]. Minimagnetospheres have been evidenced with a density cavity detected near a strong crustal magnetic source by the Lunar Prospector [*Halekas et al.*, 2008]. Chandrayaan-1 spacecraft showed evidence for substantial reduction of the backscattered hydrogen flux from the lunar surface [*Wieser et al.*, 2010] as well as high solar wind deflection efficiencies over large-scale magnetic anomalies [*Lue et al.*, 2011]. Kaguya (SELENE) observed electrons and ions reflected by magnetic mirror effects [*Saito et al.*, 2010] and by electric fields created above the anomalies due to charge separation [*Saito et al.*, 2012]. Deflection of the protons over small-scale anomalies has also been observed and attributed to electrostatic fields [*Lue et al.*, 2011]. Electrostatic solitary waves associated with lunar magnetic anomalies were reported [*Hashimoto et al.*, 2010].

[1]Laboratory for Atmospheric and Space Physics, University of Colorado Boulder, Boulder, Colorado, USA.
[2]Colorado Center for Lunar Dust and Atmospheric Studies, NASA Lunar Science Institute, Boulder, Colorado, USA.
[3]Department of Physics, University of Colorado Boulder, Boulder, Colorado, USA.

Corresponding author: X. Wang, Laboratory for Atmospheric and Space Physics, University of Colorado Boulder, Boulder, CO 80309, USA. (xu.wang@colorado.edu)


0148-0227/12/2012JA017635

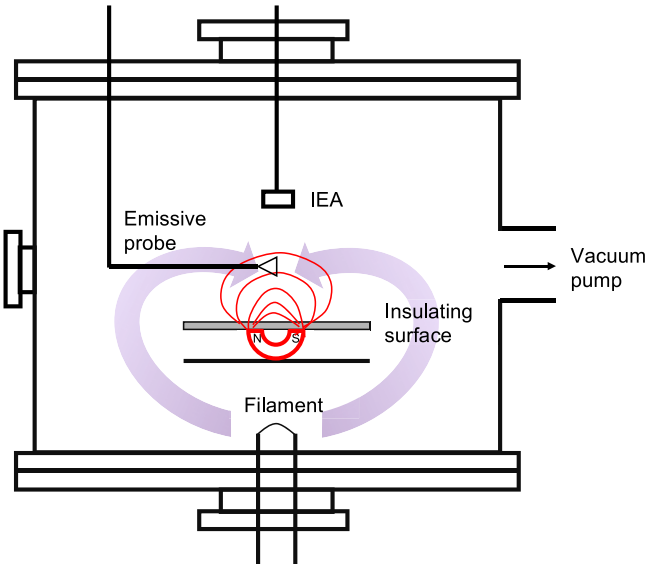


**Figure 1.** Schematic of experimental and diagnostic setup.

[3] *Siscoe and Goldstein* [1973] modeled two basic interaction modes: (1) deflected currents that close above the surface when the dipole axis is perpendicular to the surface and (2) deflected currents that intersect the lunar surface when the dipole axis is parallel to the surface. *Greenstadt* [1971] showed the conditions for maintaining asteroid magnetospheres by magnetic dipole moments. *Hood and Schubert* [1980] discussed the requirement on dipole moments for strong solar wind deflection by lunar magnetic anomalies for typical solar wind conditions. Simulations showed that the solar wind interaction with dipolar-like fields can generate a magnetosonic wake [*Omidi et al.*, 2002] or a magnetosphere with a field strength an order of magnitude stronger than the observation [*Harnett and Winglee*, 2000], and that with multiple-dipolar-like fields a minimagnetosphere will form with a smaller magnetic field strength due to the lateral extent of the magnetic field [*Harnett and Winglee*, 2003].

[4] In addition, swirl-shaped high-albedo markings observed on the lunar surface may have a strong correlation with the magnetic anomalies. One possible mechanism is that the magnetic anomalies may deflect or stand off the solar wind protons to prevent maturation of the underlying regolith [*Hood and Schubert*, 1980]. Alternatively, the transport of charged dust could also result in the redistribution of bright small-sized dust particles due to enhanced electric fields in the magnetic anomaly interaction regions [*Garrick-Bethell et al.*, 2011]. While the near-surface lunar conditions cannot be closely reproduced, for example, the high-energy solar wind flow and the complex field configurations of the magnetic anomalies, small-scale laboratory experiments are very helpful for figuring the intrinsic processes.

[5] The sheath, a transition layer between a surface and the bulk plasma in the presence of magnetic fields has been of a great interest to the plasma physics community for decades, including applications in magnetic fusion, industrial plasma processing, space and basic plasma physics, for example. The behavior of such a sheath has been characterized by a number of theoretical and experimental studies [*Krasheninnikova et al.*, 2010]. Magnetic sheaths have been examined under a variety of circumstances, including the magnetic fields parallel and oblique to the wall, in collisionless and collisional plasmas, and in the regimes of $\rho_e < \lambda_D < \rho_i$, $\lambda_D < \rho_e$ and $\lambda_D > \rho_i$, where $\rho$ is the Larmor radius of the electron/ions, and $\lambda$ is the Debye length. However, all of these studies were carried out for large-scale, global magnetic field configurations.

[6] In this paper, we show laboratory results of plasma interactions with a magnetic dipole field over an insulating surface and discuss the implications for the interactions of lunar magnetic anomalies with the solar wind plasma flow.

## 2. Experiments

[7] The experiments were conducted in a cylindrical stainless steel vacuum chamber, 28 cm high and 51 cm in diameter, shown in Figure 1. The base pressure of $10^{-6}$ Torr is obtained by a turbomolecular pump. Argon plasma is created by the impact ionization using electrons emitted from a negatively biased and heated filament in the bottom of the chamber. A metal plate above the filament prevented the primary electrons from entering the bulk plasma. A magnetic dipole field is created above an insulating surface by placing a horseshoe permanent magnet underneath. The working pressure operates from $3.0 \times 10^{-4}$ to $1.2 \times 10^{-3}$ Torr. Plasma is characterized by a cylindrical Langmuir probe inserted in the bulk region where the magnetic field is negligible. Potentials above the surface are measured using an emissive probe with a current-voltage method [*Diebold et al.*, 1988] that has advantage of acquiring data in real time. This method is calibrated with the inflection point method in the limit of zero emission, which has been demonstrated as a good measure of the potential in magnetized plasmas as well as field-free plasmas [*Smith et al.*, 1979].

[8] Magnitudes of both parallel ($B_{//}$) and perpendicular ($B_{\perp}$) components of the magnetic field were measured with a magnetic probe oriented in both directions. A vector field map, combining the two components, shows a dipolar magnetic field structure, Figure 2a. On the insulating surface the maximum strength of the magnetic field in the center of the dipole is ~550 G, and the highest magnetic field strength is ~700 G located at two cusps.

[9] The plasma density varies from $2 \times 10^7$ cm$^{-3}$ to $1.2 \times 10^8$ cm$^{-3}$, depending on the neutral pressure and the electron emission current from the filament. The current-voltage (I-V) characteristics show two electron populations, i.e., cold and hot electrons that have temperatures of 2.3 ~ 3.2 eV and 5.0 ~ 5.5 eV, respectively. The Debye length is 0.11 ~ 0.3 cm. The ion temperature is ~0.5 eV measured by a gridded retarding-field ion-energy-analyzer (IEA) [*Böhm and Perrin*, 1993], which is much hotter than the temperature of the newborn ions, i.e., the neutral gas temperature 0.025 eV. The ion heating possibly occurs during the plasma expansion from the source located in the bottom of the chamber to the top of the insulating surface as shown in Figure 1. Ambipolar electric fields form in the expansion because the hot electrons move faster and leave the cold electrons and the ions behind. The ions in turn are accelerated by the electric fields and collide with neutrals, leading to a broader energy distribution, i.e., hotter

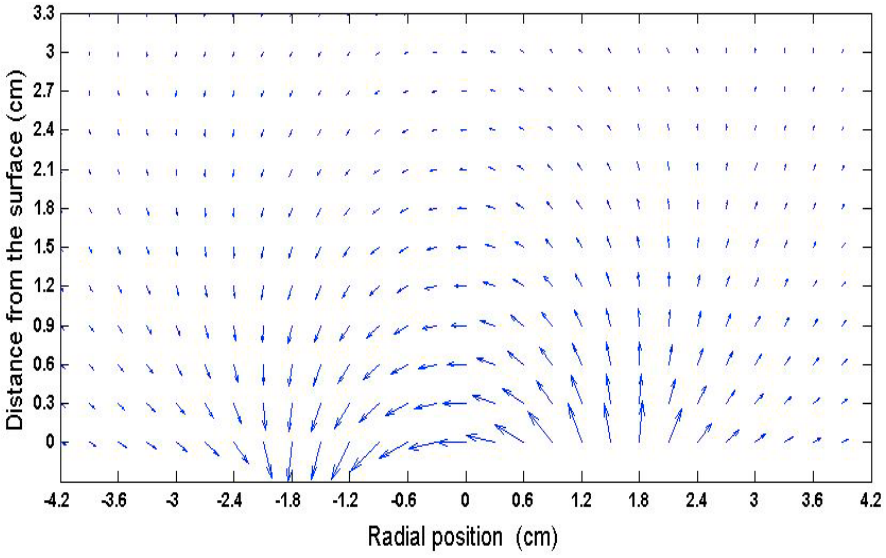


(a)

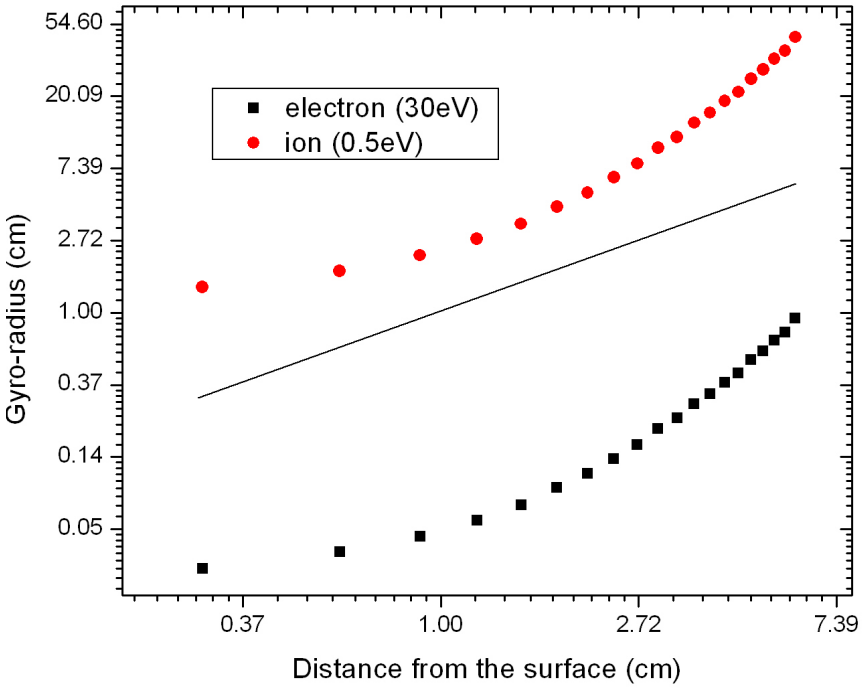


(b)

**Figure 2.** (a) Mapping of magnetic field strength; (b) gyroradii for 0.5 eV ion and 30 eV electron as a function of distance from the surface in the center of the magnetic dipole. The solid line shows the gyroradii that equal to the distances from the surface.

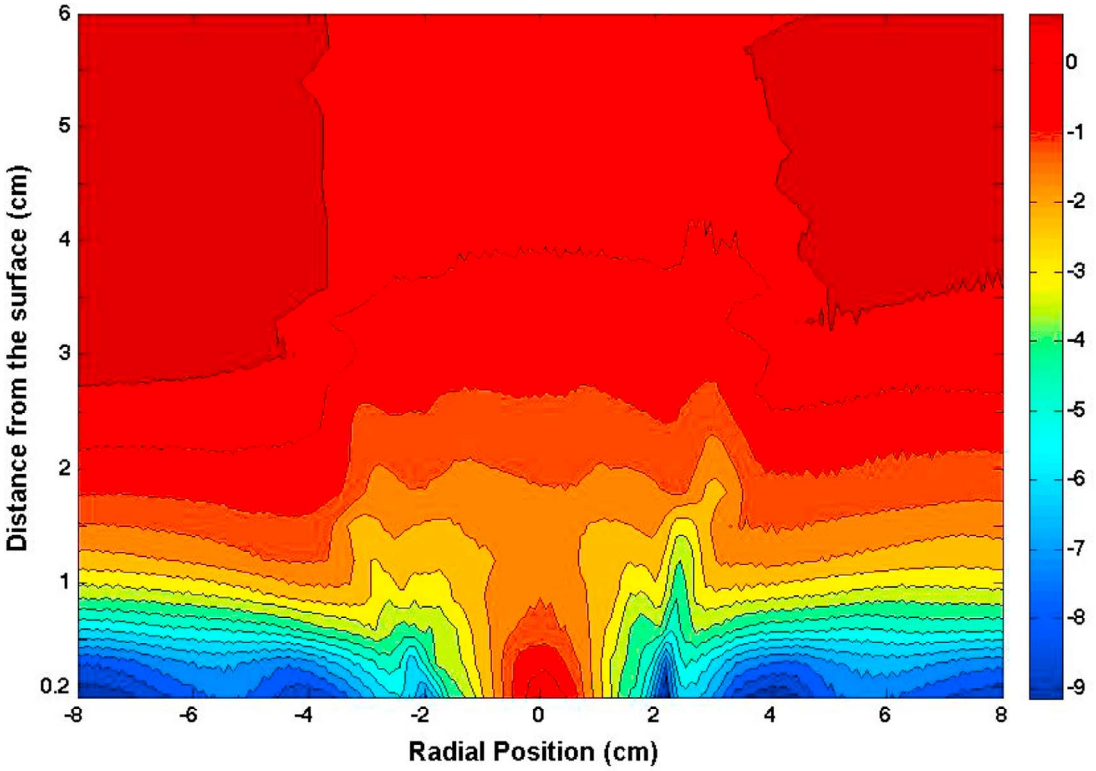


**Figure 3.** Potential contours above the surface along the dipole axis. Colors represent potentials in volts.

temperature. The ion temperature drops to ~0.23 eV by removing the metal plate and the insulating surface because the expansion effect is reduced. Gyroradii of the electrons and the ions, $r_g$ are calculated from the following equation

$$r_g = \frac{mv}{qB} \tag{1}$$

where $m$ is the mass, $v$ is the velocity, $q$ is the elementary charge and $B$ is the strength of magnetic field. Figure 2b shows the gyroradii for the 0.5 eV thermal ions and the 30 eV high-energy tail electrons as a function of the distance from the surface in the center of the magnetic dipole. The ions have gyroradii larger than the distances from the surface and are thus able to reach the surface, defined as "unmagnetized." However, even the high-energy tail electrons have gyroradii smaller than the distances from the surface, defined as "magnetized." They are shielded away from the dipole center at the height around 5.5 cm.

## 3. Results

[10] Potential contours above the insulating surface along the magnetic dipole axis are shown in Figure 3. A non-monotonic potential structure exists above the surface in the center of the dipole. The potential on the surface is slightly more positive than the bulk plasma potential and a potential minimum exists at ~1.5 cm above the surface. Horizontal potential profiles show strong variations at the surface. The surface potential is the most positive in the center of the dipole and turns more negative near the cusps.

### 3.1. Non-monotonic Sheaths

[11] In the conventional theory for the Bohm sheath, electrons with higher mobility go to a surface that is electrically floating in plasma and charge it more negatively than the bulk plasma potential, creating an electric field that attracts ions to the surface and repels electrons. However, in our experiments as described in the previous section, the electrons are magnetically shielded away at ~5.5 cm from the central surface but the unmagnetized ions go to the surface and charge the surface to be slightly more positive than the bulk potential. Instead of forming a monotonic sheath to return the ions at the surface, a potential minimum develops at ~1.5 cm above the surface, indicating the access of the electrons into the shielding region. Due to the non-uniform and curved magnetic field, the guiding centers of the gyro-electrons will drift by forces of $\nabla \mathbf{B} \times \mathbf{B}$ and $\mathbf{R_c} \times \mathbf{B}$. However, these guiding centers drift in a plane perpendicular to the dipole axis. Secondary electrons are negligible in this experiment due to the low-energy flux of the plasma electrons according to the previous experiments with the similar plasma conditions. Therefore, a more likely reason for the electrons to have access to the shielding region is scattering due to electron-electron and electron-neutral collisions. The electrons following the magnetic field lines are focused into the cusps. Electron-electron collisional rate thus significantly increases due to the increase in electron density. The collision causes the electrons to migrate across the magnetic field lines into field lines that pierce the shielding region. A small horizontal displacement across the field lines at the cusps can make a large vertical displacement above the dipole center due to the line focusing at the cusps. Electrons

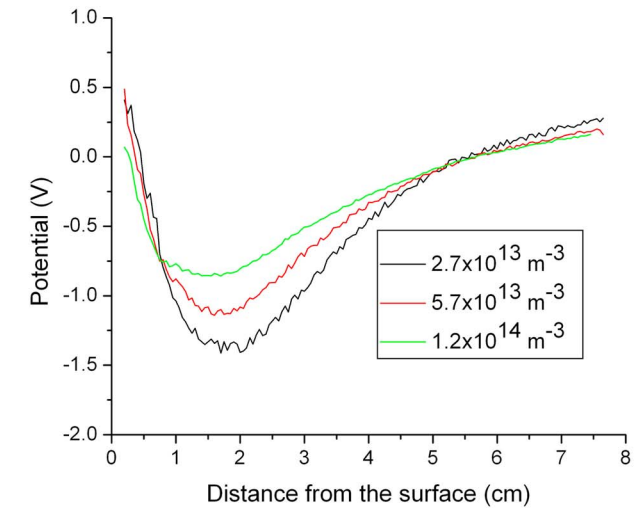


(a)

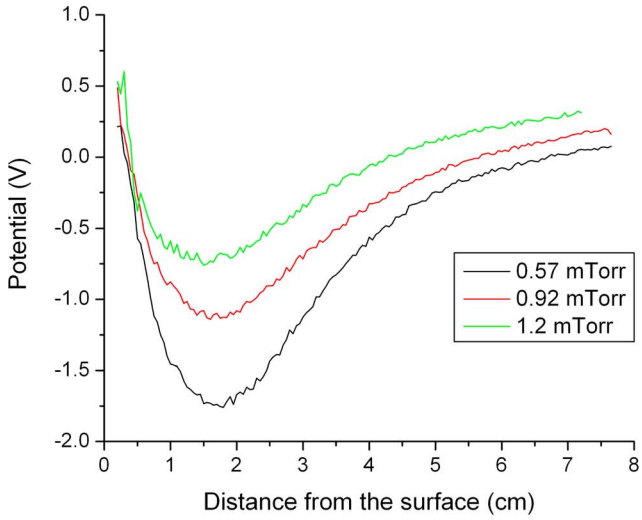


(b)

**Figure 4.** Potential profiles above the surface in the dipole center (a) with three densities in a constant pressure at 0.92 mTorr and (b) with three pressures in a constant density of $5.7 \times 10^7$ cm$^{-3}$.

gyrating around the field lines can travel a much longer distance in the plasma, leading to a higher probability for collisions with neutrals. The electrons can thus diffuse into the shielding region by the electron-neutral collision as well. The electrons with large enough pitch angles can be reflected near the cusps, where the magnetic fields are the highest, due to magnetic mirror effects, and get trapped between the two cusps in the symmetrical field configuration. The trapped electrons in the shielding region are likely the cause of the potential minimum.

[12] In order to further understand the non-monotonic sheath, potential profiles are measured above the surface in the center of the dipole as a function of the plasma density and the neutral pressure, shown in Figures 4a and 4b, respectively. The surface potentials are always slightly more positive than the bulk plasma potentials, and the sheath structures remain similar with the plasma-sheath boundary at ~5.5 cm, and the potential minimum at 1.5 ~ 1.8 cm above the surface. The position of the sheath edge is consistent with the boundary of the electron shielding region at 5.4 ~ 5.7 cm height. These results imply that the magnetic field configuration is primarily responsible for setting up the spatial structure of the sheath. The only significant variation is that the value of the potential minimum with respect to the bulk plasma potential decreases with increasing plasma density and neutral pressure, Figure 5. The increasing rate of electron-electron and electron-neutral collisions wash out the spatial structure of the potential distribution, hence, reduce the electric fields in the sheath.

### 3.2. Spatial Variations of the Surface Potential

[13] Potentials on the surface vary along the dipole axis as shown in Figure 6a. The four positive and negative potential peaks are marked in Figure 6a. To identify these peaks, a sketch is made in Figure 6b to show the ion and electron trajectories. The potential is the most positive in the center because of the ion charging as described in the previous section (Peak I - "Electron shielding"). The surfaces in the cusps are charged more negatively because the magnetized electrons following the field lines are focused into the cusps (Peak II - "Electron focusing"). The electron gyroradius increases radially along the dipole axis because of the decrease in magnetic field strength, Figure 6c. When the electrons follow the field lines to the distance 0.15 cm from the surface, the gyroradius is as large as 0.1–0.16 cm at

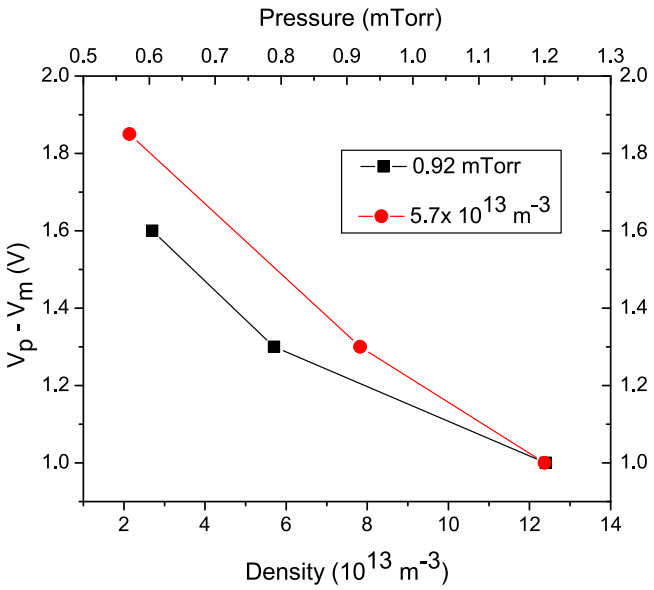


**Figure 5.** The value of the potential minimum $V_m$ with respect to the bulk plasma potential $V_p$ as a function of the density and the pressure, respectively.

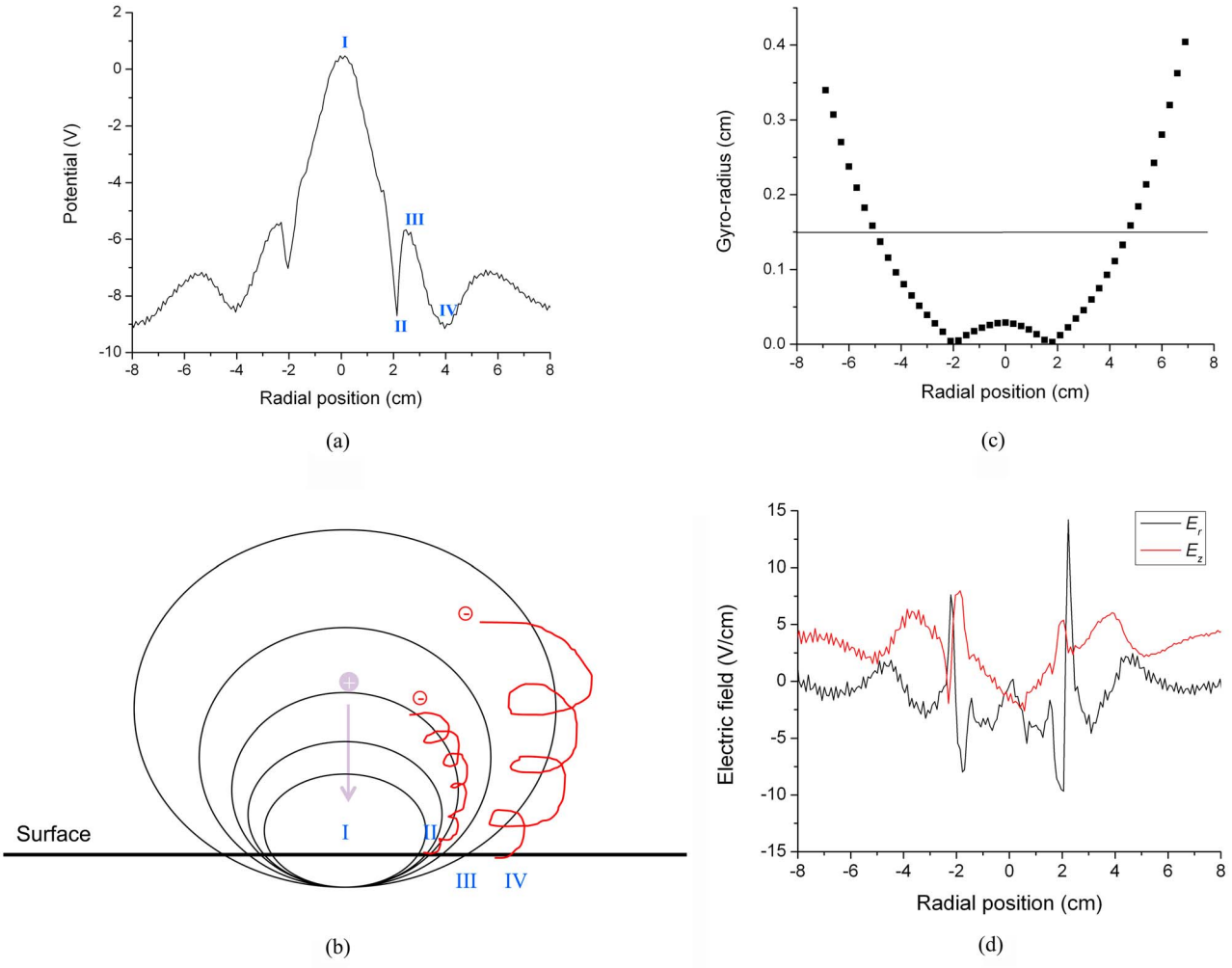


**Figure 6.** (a) Horizontal potential profile on the surface along the dipole axis. Peaks are marked as I, II, III and IV. (b) A sketch of ion and electron trajectories. (c) Horizontal profile of the electron gyroradius at 0.15 cm from the surface. (d) Horizontal and vertical electric fields on the surface along the dipole axis. $E_r$ and $E_z$ represent radial and vertical electric fields, respectively. $E_r$ points inward when $E_r > 0$ and points outward when $E_r < 0$; $E_z$ points downward when $E_z > 0$ and points upward when $E_z < 0$.

radial position 4.0–5.0 cm. The electrons can thus intercept the surface before the field line reaches the surface, charging the surface more negatively (Peak IV - "Electron intercepting"). Both processes of the electron focusing at the peak II and the electron intercepting at the peak IV will cause less electrons to reach the region between these two peak regions, resulting in a slightly more positive surface potential therein (Peak III - "Electron shadowing"). The electric fields on the surface along the dipole axis are derived from the potential measurements shown in Figure 3 and are shown in Figure 6d, indicating enhancements for both horizontal and vertical components in the cusp regions. The surface charge density is determined by balancing the currents from electrons and ions. In a magnetic dipole field with magnetized electrons, the electron current is affected by many effects including their bounce-motion between reflecting mirror points, field-line focusing, guiding-center drifts, and reflection from potential barriers. Hence, the complex spatial structure of the sheath is not unexpected. Computer simulation work will be helpful for a more complete understanding of these observations. While likely different in detail, similarly complex sheath structure can be expected near magnetic anomalies on the lunar surface.

## 4. Implications and Discussion

[14] As described in section 1, efficient solar wind deflection is observed over strong, coherent large-scale magnetic anomalies (3 nT at 100 km altitude and >1000 km in diameter). These interactions are well approximated with MHD theories and simulations. The solar wind will stand off when the magnetic pressure balances the solar wind dynamic pressure by the following equation

$$nmv^2 = B^2/8\pi \quad (2)$$

where $n$ is the density, $m$ is the mass, $v$ is the flow velocity and $B$ is the strength of magnetic field. However, deflection

is also observed over weak, isolated, dipole-like small-scale anomalies (3 nT at 30 km altitude and <100 km in diameter) [*Lue et al.*, 2011], where the solar wind electrons are magnetized with a smaller gyroradius of 6 km but the protons are unmagnetized with a larger gyroradius of 1100 km. In such regions, MHD approximations break down and the kinetic effects become more important, which is analogous to our experiments.

[15] It is thus expected that the lunar surface in the small-scale magnetic anomaly regions can be charged as high as several hundred volts positive due to the high energy of the solar wind protons (~keV), creating an electric field to reflect the low-energy fraction of the protons. Similarly, the solar wind protons may be electrostatically deflected by an ambipolar electric field resulting from a charge separation above the surface [*Lue et al.*, 2011; *Saito et al.*, 2012], instead of on the surface as shown in our experiments. Solar wind electrons will be unlikely to enter the electron-shielding region due to the weak electron-electron collision for the low density of the solar wind electrons and a lack of the electron-neutral collision. However, the non-monotonic sheaths may still form in the anomaly regions because photoelectrons and secondary electrons emitted from the lunar surface can follow the field lines into the shielding region and get trapped.

[16] Electric fields are also expected to be stronger in the regions where the solar wind interacts with the magnetic anomalies. Even small-scale magnetic anomalies have more complex magnetic field distributions due to crustal magnetization than that of a simple dipole. The distribution of the electric field is thus expected to be more complex than shown in our experiments. As a consequence, fine-sized high-albedo dust particles maybe re-sorted to form unusual, swirl-like patterns. Further laboratory studies on dust dynamics in our setup is planned to verify dust transport near magnetic anomalies, as a possible model for the formation of lunar swirls.

## 5. Conclusions

[17] We studied the plasma interaction with a magnetic dipole field over an insulating surface for the case of the magnetized electrons and unmagnetized ions. The emergence of non-monotonic sheaths and complex potential variations along the dipole axis have been identified. The potential on the surface in the dipole center was found to be slightly more positive than the bulk plasma potential due to the ion charging, while the electrons remained shielded away. The experiments showed that both electron-electron and electron-neutral collisions can cause the electrons to migrate into the shielding region. A potential minimum is thus formed when these electrons are trapped between the symmetrical cusps due to the magnetic mirror effects. The potential variations on the surface are a consequence of the inhomogeneous dipolar field, showing an electric field enhancement at the cusps. The laboratory results show that the charge separation could occur at the lunar surface in the regions where the solar wind interacts with the small-scale magnetic anomalies, leading the surface to charge to large positive values in order to reflect a fraction of the incoming protons. At the Moon, a non-monotonic sheath may also form due to the photoelectrons and secondary electrons trapped in the electron-shielding region. The enhanced electric fields in such regions may increase dust transport, possibly explaining lunar swirl formation.

[18] **Acknowledgments.** This work was supported by the NASA's LASER program (NNX08AY77G) and by the NASA Lunar Science Institute's Colorado Center for Lunar Dust and Atmospheric Studies (CCLDAS).

[19] Philippa Browning thanks the reviewers for their assistance in evaluating this paper.

## References

Barnes, A., P. Cassen, J. P. Mihalov, and A. Eviatar (1971), Permanent lunar surface magnetism and its deflection of the solar wind, *Science*, *172*, 716–718, doi:10.1126/science.172.3984.716.

Böhm, C., and J. Perrin (1993), Retarding-field analyzer for measurements of ion energy-distributions and secondary-electron emission coefficients in low-pressure radio-frequency discharges, *Rev. Sci. Instrum.*, *64*, 31–44, doi:10.1063/1.1144398.

Colburn, D. S., R. G. Currie, J. P. Mihalov, and C. P. Sonett (1967), Diamagnetic solar wind cavity discovered behind the moon, *Science*, *158*, 1040–1042, doi:10.1126/science.158.3804.1040.

Colburn, D. S., J. P. Mihalov, and C. P. Sonett (1971), Magnetic observations of the lunar cavity, *J. Geophys. Res.*, *76*(13), 2940–2957, doi:10.1029/JA076i013p02940.

Diebold, D., N. Hershkowitz, A. D. Bailey III, M. H. Cho, and T. Intrator (1988), Emissive probe current bias method of measuring dc vacuum potential, *Rev. Sci. Instrum.*, *59*, 270–275, doi:10.1063/1.1140239.

Dyal, P., C. W. Parkin, C. P. Sonett, R. L. DuBois, and G. Simmons (1971), Lunar portable magnetometer experiment, in *Apollo 14 Preliminary Science Report*, *NASA Spec. Publ.*, *NASA SP-272*, 227.

Garrick-Bethell, I., J. W. Head III, and C. M. Pieters (2011), Spectral properties, magnetic fields, and dust transport at lunar swirls, *Icarus*, *212*, 480–492, doi:10.1016/j.icarus.2010.11.036.

Greenstadt, E. W. (1971), Conditions for magnetic interaction of asteroids with the solar wind, *Icarus*, *14*, 374–381, doi:10.1016/0019-1035(71)90008-X.

Halekas, J. S., D. L. Mitchell, R. P. Lin, S. Frey, L. L. Hood, M. H. Acuna, and A. B. Binder (2001), Mapping of crustal magnetic anomalies on the lunar nearside by the Lunar Prospector electron reflectometer, *J. Geophys. Res.*, *106*, 27,841–27,852, doi:10.1029/2000JE001380.

Halekas, J. S., D. A. Brain, D. L. Mitchell, R. P. Lin, and L. Harrison (2006), On the occurrence of magnetic enhancements caused by solar wind interaction with lunar crustal fields, *Geophys. Res. Lett.*, *33*, L08106, doi:10.1029/2006GL025931.

Halekas, J. S., G. T. Delory, D. A. Brain, R. P. Lin, and D. L. Mitchell (2008), Density cavity observed over a strong lunar crustal magnetic anomaly in the solar wind: A mini-magnetosphere?, *Planet. Space Sci.*, *56*, 941–946, doi:10.1016/ j.pss.2008.01.008.

Harnett, E. M., and R. M. Winglee (2000), Two-dimensional MHD simulations of the solar wind interaction with magnetic field anomalies on the surface of the Moon, *J. Geophys. Res.*, *105*, 24,997–25,007, doi:10.1029/2000JA000074.

Harnett, E. M., and R. Winglee (2003), 2.5-D simulations of the solar wind interacting with multiple dipoles on the surface of the Moon, *J. Geophys. Res.*, *108*(A2), 1088, doi:10.1029/2002JA009617.

Hashimoto, K., et al. (2010), Electrostatic solitary waves associated with magnetic anomalies and wake boundary of the Moon observed by KAGUYA, *Geophys. Res. Lett.*, *37*, L19204, doi:10.1029/2010GL044529.

Hood, L. L., and G. Schubert (1980), Lunar magnetic anomalies and surface optical properties, *Science*, *208*, 49–51, doi:10.1126/science.208.4439.49.

Hood, L. L., A. Zakharian, J. Halekas, D. L. Mitchell, R. P. Lin, M. H. Acuna, and A. B. Binder (2001), Initial mapping and interpretation of lunar crustal magnetic anomalies using Lunar Prospector magnetometer data, *J. Geophys. Res.*, *106*, 27,825–27,839, doi:10.1029/2000JE001366.

Krasheninnikova, N. S., X. Tang, and S. Roytershteyn (2010), Scaling of the plasma sheath in a magnetic field parallel to the wall, *Phys. Plasmas*, *17*, 057103, doi:10.1063/1.3354106.

Lin, R. P., D. L. Mitchell, D. W. Curtis, K. A. Anderson, C. W. Carlson, J. McFadden, M. H. Acuna, L. L. Hood, and A. Binder (1998), Lunar surface magnetic fields and their interaction with the solar wind: Results from Lunar Prospector, *Science*, *281*, 1480–1484, doi:10.1126/science.281.5382.1480.

Lue, C., Y. Futaana, S. Barabash, M. Wieser, M. Holmstrom, A. Bhardwaj, M. Dhanya, and P. Wurz (2011), Strong influence of lunar crustal fields

on the solar wind flow, *Geophys. Res. Lett.*, *38*, L03202, doi:10.1029/2010GL046215.

Lyon, E. F., H. S. Bridge, and J. H. Binsack (1967), Explorer 35 plasma measurements in the vicinity of the moon, *J. Geophys. Res.*, *72*(23), 6113–6117, doi:10.1029/JZ072i023p06113.

Mitchell, D. L., J. S. Halekas, R. P. Lin, S. Frey, L. L. Hood, M. H. Acuña, and A. Binder (2008), Global mapping of lunar crustal magnetic fields by Lunar Prospector, *Icarus*, *194*, 401–409, doi:10.1016/j.icarus.2007.10.027.

Ness, N. F., K. W. Behannon, C. S. Scearce, and S. C. Cantarano (1967), Early results from the magnetic field experiment on lunar Explorer 35, *J. Geophys. Res.*, *72*(23), 5769–5778, doi:10.1029/JZ072i023p05769.

Ness, N. F., K. W. Behannon, H. E. Taylor, and Y. C. Whang (1968), Perturbations of the interplanetary magnetic field by the lunar wake, *J. Geophys. Res.*, *73*(11), 3421–3440, doi:10.1029/JA073i011p03421.

Omidi, N., X. Blanco-Cano, C. T. Russell, H. Karimabadi, and M. Acuna (2002), Hybrid simulations of solar wind interaction with magnetized asteroids: General characteristics, *J. Geophys. Res.*, *107*(A12), 1487, doi:10.1029/2002JA009441.

Russell, C. T., and B. R. Lichtenstein (1975), On the source of lunar limb compression, *J. Geophys. Res.*, *80*(34), 4700–4711, doi:10.1029/JA080i034p04700.

Saito, Y., et al. (2010), In-flight performance and initial results of Plasma Energy Angle and Composition Experiment (PACE) on SELENE (Kaguya), *Space Sci. Rev.*, *154*, 265–303, doi:10.1007/s11214-010-9647-x.

Saito, Y., M. N. Nishino, M. Fujimoto, T. Yamamoto, S. Yokota, H. Tsunakawa, H. Shibuya, M. Matsushima, H. Shimizu, and F. Takahashi (2012), Simultaneous observation of the electron acceleration and ion deceleration over lunar magnetic anomalies, *Earth Planets Space*, *64*(2), 83–92, doi:10.5047/eps.2011.07.011.

Siscoe, G. L., and B. Goldstein (1973), Solar wind interaction with lunar magnetic fields, *J. Geophys. Res.*, *78*, 6741–6748, doi:10.1029/JA078i028p06741.

Smith, J. R., N. Hershkowitz, and P. Coakley (1979), Inflection-point method of interpreting emissive probe characteristics, *Rev. Sci. Instrum.*, *50*, 210–218, doi:10.1063/1.1135789.

Taylor, H. E., K. W. Behannon, and N. F. Ness (1968), Measurement of the perturbed interplanetary magnetic field in the lunar wake, *J. Geophys. Res.*, *73*(21), 6723–6735, doi:10.1029/JA073i021p06723.

Wieser, M., S. Barabash, Y. Futaana, M. Holmstrom, A. Bhardwaj, R. Sridharan, M. B. Dhanya, P. Wurz, A. Schaufelberger, and K. Asamura (2010), First observation of a mini-magnetosphere above a lunar magnetic anomaly using energetic neutral atoms, *Geophys. Res. Lett.*, *37*, L05103, doi:10.1029/2009GL041721.